

Dynamic mesoscopic response mechanism of rubberised epoxy asphalt trackbed subjected to high-speed train loading

Shi, Chenguang; Wu, You; Yan, Guihao; Xu, Yang; Guo, Peng; Yang, Jun

DOI

[10.1080/10298436.2025.2556978](https://doi.org/10.1080/10298436.2025.2556978)

Publication date

2025

Document Version

Final published version

Published in

International Journal of Pavement Engineering

Citation (APA)

Shi, C., Wu, Y., Yan, G., Xu, Y., Guo, P., & Yang, J. (2025). Dynamic mesoscopic response mechanism of rubberised epoxy asphalt trackbed subjected to high-speed train loading. *International Journal of Pavement Engineering*, 26(1), Article 2556978. <https://doi.org/10.1080/10298436.2025.2556978>

Important note

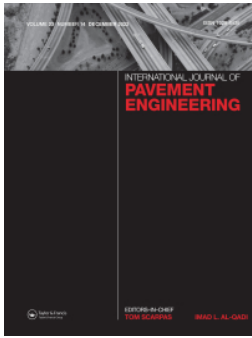
To cite this publication, please use the final published version (if applicable).
Please check the document version above.

Copyright

Other than for strictly personal use, it is not permitted to download, forward or distribute the text or part of it, without the consent of the author(s) and/or copyright holder(s), unless the work is under an open content license such as Creative Commons.

Takedown policy

Please contact us and provide details if you believe this document breaches copyrights.
We will remove access to the work immediately and investigate your claim.



Dynamic mesoscopic response mechanism of rubberised epoxy asphalt trackbed subjected to high-speed train loading

Chenguang Shi, You Wu, Guihao Yan, Yang Xu, Peng Guo & Jun Yang

To cite this article: Chenguang Shi, You Wu, Guihao Yan, Yang Xu, Peng Guo & Jun Yang (2025) Dynamic mesoscopic response mechanism of rubberised epoxy asphalt trackbed subjected to high-speed train loading, International Journal of Pavement Engineering, 26:1, 2556978, DOI: [10.1080/10298436.2025.2556978](https://doi.org/10.1080/10298436.2025.2556978)

To link to this article: <https://doi.org/10.1080/10298436.2025.2556978>



© 2025 The Author(s). Published by Informa UK Limited, trading as Taylor & Francis Group.



Published online: 10 Sep 2025.



[Submit your article to this journal](#)



Article views: 184

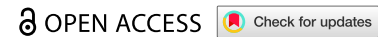


[View related articles](#)



[View Crossmark data](#)

RESEARCH ARTICLE



Dynamic mesoscopic response mechanism of rubberised epoxy asphalt trackbed subjected to high-speed train loading

Chenguang Shi^a, You Wu^b , Guihao Yan^c, Yang Xu^d, Peng Guo^a and Jun Yang^e

^aNational & Local Joint Engineering Research Center of Transportation and Civil Engineering Materials, Chongqing Jiaotong University, Chongqing, China; ^bSection of Railway Engineering, Delft University of Technology, Delft, The Netherlands; ^cChinese Academy of Quality and Inspection & Testing, Beijing, China; ^dRailway Engineering Research Institute, China Academy of Railway Sciences Corporation Limited, Beijing, China; ^eSchool of Transportation, Southeast University, Nanjing, PR China

ABSTRACT

Rubberized epoxy asphalt trackbeds, incorporating crumb rubber (CR) particles within the cured matrix, demonstrate superior vibration damping and deformation resistance characteristics. Current research remains predominantly focused on macroscopic properties, leaving a critical knowledge gap regarding the particulate-scale mechanisms controlling their dynamic performance under high-speed rail loading. This study bridges this gap through advanced discrete element modeling, developing two-dimensional DEM representations of four sleeper-asphalt composite units with varying CR concentrations (0%, 2%, 4%, and 6%). The models demonstrate exceptional validation accuracy against finite element analyses, with track stiffness predictions within 96.7–152.4 kN/mm range (maximum deviation <2.07%). Our particle-scale investigation of 350 km/h loading cycles reveals three key phenomena: (1) CR content proportionally increases dynamic deformation (stabilizing at 0.5 mm for 6% CR after three loading cycles), while simultaneously enhancing elastic recovery and cumulative deformation resistance; (2) CR particles redistribute contact forces (0–100 N), with 4% content as a critical threshold shifting behavior from aggregate-dominated to CR-controlled; (3) This transition optimizes stress distribution and force chain homogeneity, achieving optimal balance between flexibility and stability. The findings provide essential insights for designing high-performance rubber-modified railway trackbeds.

ARTICLE HISTORY

Received 6 July 2025

Accepted 31 August 2025





KEYWORDS

Rubberised epoxy asphalt trackbed; discrete element method (DEM); dynamic response mesoscopic mechanism

1. Introduction

Traditional railway tracks are broadly classified into ballasted and ballastless systems, differentiated by their substructure composition (Shi et al., 2021). Ballasted tracks employ a granular ballast bed, offering advantages such as elasticity, efficient load distribution, and simplified maintenance (Fang et al., 2024); however, dynamic loads induce particle rearrangement, degradation, and eventual track geometry deterioration (Charoenwong et al., 2024; Heydari et al., 2024; Malisetty & Indraratna, 2024; Paz et al., 2024). In contrast, ballastless tracks utilise concrete slabs, ensuring structural integrity, minimal maintenance, and geometric stability, albeit at the cost of reduced elasticity, heightened wheel-rail vibrations, and environmental noise (Gruetzmacher et al., 2025; Jin et al., 2025; Zhao et al., 2024). In summary, while ballasted tracks demonstrate superior adaptability to dynamic loads, their susceptibility to ballast particle abrasion necessitates frequent maintenance. Conversely, the higher rigidity of ballastless tracks results in more pronounced vibrations that significantly impact both track structures and the surrounding environment.

To address these challenges, researchers have explored the application of polyurethane (Jing et al., 2019; Xiao et al., 2020; Xiong et al., 2021; Xu et al., 2024), epoxy resin (Liu et al., 2018; Shi et al., 2021; Wu et al., 2023), and asphalt-based binding agents (Fang et al., 2017, 2020; Ramirez Cardona et al., 2020; Wang et al., 2022, 2025; Xiao et al., 2021) to enhance the interparticle bonding of aggregate materials, thereby

CONTACT You Wu  You.Wu@tudelft.nl  Section of Railway Engineering, Delft University of Technology, Stevinweg 1, 2628 CN, Delft, The Netherlands; Jun Yang  yangjun@seu.edu.cn  School of Transportation, Southeast University, #2 Southeast University Road, Nanjing, PR China

© 2025 The Author(s). Published by Informa UK Limited, trading as Taylor & Francis Group.

This is an Open Access article distributed under the terms of the Creative Commons Attribution License (<http://creativecommons.org/licenses/by/4.0/>), which permits unrestricted use, distribution, and reproduction in any medium, provided the original work is properly cited. The terms on which this article has been published allow the posting of the Accepted Manuscript in a repository by the author(s) or with their consent.

improving their mechanical performance. Compared with conventional binding materials, polyurethane foam effectively consolidates loose ballast particles into an integrated structure, significantly reducing residual deformation in the ballast bed (Jing et al., 2019). The low-stiffness characteristics of polyurethane foam maintain the system's elasticity while preventing particle displacement. Furthermore, the foam's expansive properties enable complete void filling between particles, mitigating ballast fouling from external contaminants such as dust, sand, and debris (Alam & Hussaini, 2023; Gundavaram & Hussaini, 2023a, 2023b; Liu et al., 2022b; Zhang et al., 2023, 2024). In contrast to polyurethane-stabilised ballast tracks, asphalt trackbeds utilise asphalt mixture composites as structural layers to entirely replace traditional granular ballast systems, which is technically termed as asphalt overlayment (AOL) (Fang et al., 2020; Ramirez Cardona et al., 2020). Similarly, Bose et al. (2020, 2021) termed this structure as a 'ballastless asphalt track'. Their research team constructed a full-scale experimental track section within a confined steel container, as illustrated in Figure 1a. The test setup featured a three-layer supporting structure: (1) an asphalt mixture trackbed layer at the surface, (2) an unbound granular layer (UGL) as the intermediate layer, and (3) a rubber isolation mat at the base to simulate subgrade and foundation conditions. It investigates the mechanical response of ballastless asphalt track (BAT) through controlled laboratory experiments, with a focus on their performance under vertical loading and isothermal conditions (Bose et al., 2020). Unlike the aforementioned continuous asphalt trackbed, the authors propose a prefabricated epoxy asphalt trackbed structure. It consists of a flat-shaped unit, including one sleeper and two prefabricated asphalt mixture blocks, which facilitate the construction and maintenance processes. A schematic diagram of the prefabricated epoxy asphalt trackbed structure is shown in Figure 1b, the height of the prefabricated asphalt mixture block is 35 cm, the width is 50 cm, and the length is 100 cm (Shi et al., 2021, 2022, 2024a; Wu et al., 2023). To enhance the vibration-damping performance of the asphalt trackbed, an epoxy asphalt mixture was prepared using a dry-process modification method with crumb rubber (CR). Over the past few decades, several researchers have conducted field tests and laboratory experiments, demonstrating that incorporating an asphalt layer can significantly enhance the safety and stability of the track bed (Bian et al., 2023; Bose et al., 2020; Gundavaram & Hussaini, 2023a, 2023b; Lee et al., 2016, 2021, 2023; Liu et al., 2022b; Shi et al., 2022; Wang et al., 2022; Zhang et al., 2023, 2024).

The elastic cured trackbed prepared with cementitious materials is a new type of track structure that lies between ballasted and ballastless tracks. Due to the presence of binding materials, the aggregates form an integrated whole, enhancing the overall stability and damping characteristics of the ballast bed. At the same time, it exhibits mechanical responses different from those of the aforementioned two types of trackbed structures. To elucidate the mechanical response of the elastic cured trackbed, finite-element method (FEM) has become the preferred method for many scholars. This approach enables a comprehensive description of the entire structure, including accurate geometric representation of both rails and track components – a distinct advantage over analytical models that rely on simplified representations (Khairallah et al., 2022). Liu et al. (2018) established a FEM of the epoxy asphalt-based concrete railway substructure (EAC-S) and investigated its structural performance. The results show that the three types of epoxy asphalt-based concretes (EACs) are all suitable for the substructure of high-speed railways and can improve the crack resistance and deformation capacity of the substructure. A 3D mechanical model of a ballastless asphalt track mockup was developed by Bose et al. in ABAQUS, with most parameters calibrated through lab tests and a few from the mockup itself (Bose et al., 2021). The validated model indicated that during a simulated train passage, the substructure experiences low vertical deformations, with the majority in the rail pad and the peak stresses and strains well below design limits. Fang et al. (2022) proposed a coarse-graded dense asphalt mixture suitable for APT (Asphalt Pavement Track, a type of ballastless track) and conducted a FEM numerical analysis of the mechanical properties of APT under high-speed train loads. The results show that the greater the structural stiffness of the APT, the stronger the control on dynamic deformation of each layer in the subgrade, and the influence on the formation is weaker than that on the bottom layer of the subgrade. Shi et al. (2024a) evaluate the feasibility and vibration attenuation of the precast rubberised epoxy asphalt trackbed via a 3D FEM simulation at a speed of 350 km/h. The FEM results indicate that the designed rubberised epoxy asphalt trackbed satisfies the design criteria, and the components of the EA-4CR track structure exhibit superior vibration reduction performance compared to other cases with the same increase in CR content. It is important to note that aforementioned studies have primarily been grounded in the

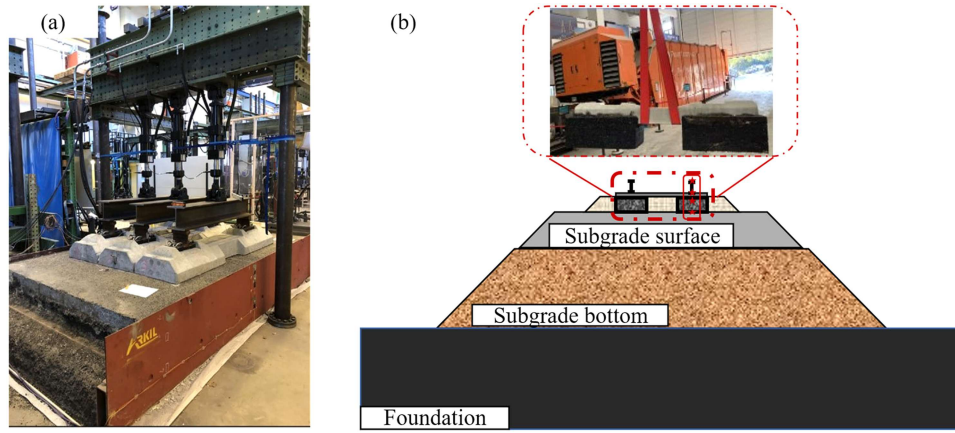


Figure 1. Asphalt trackbeds: (a) Ballastless asphalt track (Bose et al., 2020, 2021) and (b) Prefabricated rubberised epoxy asphalt trackbed (Shi et al., 2024a).

theory of continuous mechanics, with a focus on how the asphalt layer affects the overall response of the track bed or subgrade at the macro level.

Research on the mechanical properties of asphalt trackbeds has progressed significantly, transitioning from macroscopic mechanical analysis to a more sophisticated investigation of its mesoscopic mechanical behaviour. The mesoscale behaviour characterises particle-level interactions, typically spanning dimensions from 0.01 to 100 mm. Key aspects include contact force, particle displacement, and velocity (Bian et al., 2023). The discrete element method (DEM) has significantly advanced the understanding of the mesoscopic mechanical behaviour of asphalt mixtures over the years (Liu et al., 2021, 2022a, 2023a, 2023b; Luan et al., 2021; Wang et al., 2023). It provides distinct advantages for simulating asphalt trackbeds, particularly in capturing particle-scale mechanisms that govern macroscopic mechanical behaviour. However, existing DEM studies have largely overlooked the critical influence of aggregate characteristics on the mesoscopic mechanical response of asphalt trackbeds, with only sparse literature addressing this fundamental aspect.

Consequently, this study aims to evaluate the influence of CR content on the dynamic mesoscopic response mechanisms of rubberised epoxy asphalt trackbed structures under high-speed train loading conditions. Based on previous research by the authors, DEM model was developed to simulate prefabricated rubberised epoxy asphalt trackbed structures with different CR content. The model was validated through comparative analysis of track stiffness between DEM simulations and FEM results from previous study. The validated DEM model was subsequently employed to investigate cyclic deformation behaviour and dynamic response characteristics of aggregate, including interparticle contact forces, spatial distribution of particle velocities, and displacement patterns. Finally, parametric studies were conducted to provide theoretical guidance for the optimal design of rubberised epoxy asphalt trackbed systems in high-speed railway applications.

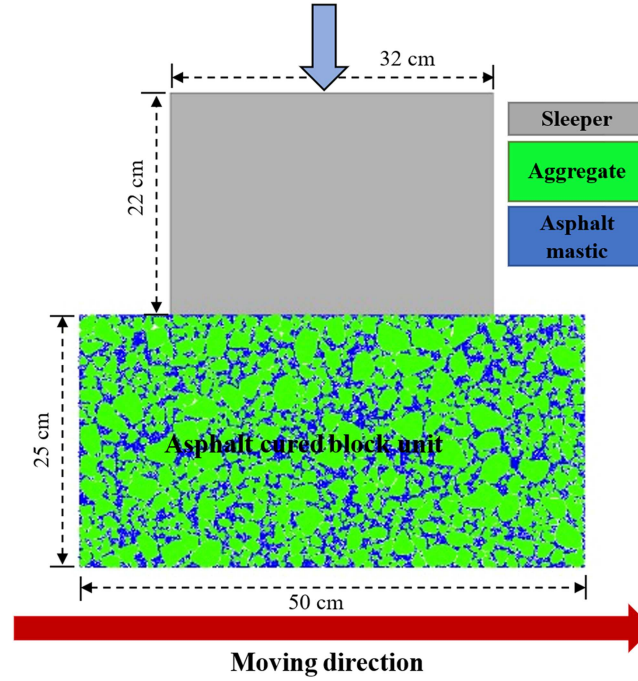
2. Two-dimensional DEM of rubberised epoxy asphalt elastic cured trackbed unit structure

2.1. DEM of the sleeper-asphalt mixture block unit structures

In this study, four types of rubberised epoxy asphalt trackbed DEM models were developed. The theoretical gradation curves for these mixtures used in trackbeds are summarised in Table 1. CR particles with a nominal size of 4.75 mm were employed to replace mineral aggregates of equivalent size through an equal-volume substitution approach, thereby maintaining consistent overall gradation characteristics. Four mixture variants were formulated with varying CR contents, designated as EA-0CR, EA-2CR, EA-4CR, and EA-6CR, where the numerical prefixes indicate the percentage of CR by total aggregate mass. These terms denote the respective asphalt trackbeds in the following analysis. The complete gradation design

Table 1. Design of rubberised epoxy asphalt mixture gradation with different CR contents.

Sieve size (mm)	26.5	19.0	16.0	13.2	9.5	4.75	CR	1.18	0.6	0.3	0.15	0.075	Filler
EA-0CR						18.53	0						
EA-2CR						13.54	2						
EA-4CR	13.25	9.50	8.86	9.58	12.79	8.54	4	7.41	5.31	4.00	2.93	2.14	5.86
EA-6CR						3.54	6						

**Figure 2.** DEM of prefabricated sleeper-asphalt mixture block unit structure.

methodology and comprehensive material properties for these asphalt mixtures have been documented in previous publications (Shi et al., 2024a, 2024b).

Figure 2 shows the DEM model of the prefabricated sleeper-asphalt mixture block unit structure of EA-0CR. This model simulates solely the force state of a single sleeper side and its corresponding asphalt block unit along the direction of motion. Firstly, a DEM model of an rubberised epoxy asphalt mixture block with a width of 50 cm and a height of 25 cm was constructed by arranging coarse aggregate clusters according to the gradation of the asphalt mixture to form a skeletal structure. Subsequently, 0.6-mm disk elements were generated in a hexagonal close packing arrangement within the specimen boundaries, and overlapping particles were removed based on their spatial relationship with the clustered pebbles. Although this method efficiently generates a particle system, it may lead to significant interfacial gaps between the disk elements and aggregate clusters. To address this, an iterative contact verification process was adopted: particles with fewer than two contacts underwent radial expansion to enhance interfacial connectivity, thereby ensuring effective bonding between the asphalt mastic and coarse aggregates. Given the skeleton-dense structure characteristics of rubberised epoxy asphalt mixtures, irregular coarse aggregates in the initial virtual specimen may induce stress concentration phenomena. A boundary servo mechanism was employed to mitigate these localised stress anomalies, ultimately optimizing the contact distribution to achieve an ideal mixture system state that balances geometric accuracy and computational feasibility. Upon completion of the asphalt block model, a sleeper with dimensions of 32 cm (width) \times 22 cm (height) was positioned at the central top region, where clump model was employed for its representation. To increase the number of contacts between the sleeper pebbles and the particles of asphalt block, intersection angle (distance) and the ratio of the minimum to maximum radii (ratio) of the sleeper clump were set to 180 and 0.1, respectively.

Table 2. Material parameters.

Material	Poisson's ratio	Friction coefficient	Stiffness ratio	Elastic modulus (MPa)
Aggregate	0.2	0.5	1.13	52,667
CR	0.45	0.98	1.41	17
Asphalt mastic	0.25	0.98	1.17	187

Table 3. Linear contact parameters in DEM models.

Contact type	Poisson's ratio	Friction coefficient	Stiffness ratio	Contact young's modulus (MPa)
A-C	0.45	0.5	1.41	33
C-M	0.44	0.98	1.39	30
A-M	0.25	0.5	1.17	372

Note: A, C and M represent the Aggregate, the CR, and the mastic, respectively.

The prefabricated rubberised epoxy asphalt cured trackbed unit structure bonds the sleeper and the asphalt mixture block into an integrated unit using epoxy asphalt mortar. For asphalt cured block unit containing asphalt mastic and coarse aggregate, the former is modelled as a densely packed assembly of uniformly sized disc elements and the latter is represented by a clump – an assembly of discs. The intersection angle (distance) and the ratio of the minimum to maximum radii (ratio) of coarse aggregate clump are 150 and 0.2, respectively. The selection of these parameter values could balance the realism of the geometric form with the efficiency of numerical simulation. For EA-2CR, EA-4CR and EA-6CR, a portion of the 4.75 mm coarse aggregates was replaced with CR according to the gradation information provided in Table 1.

To ensure consistent deformation characteristics between the DEM and FEM simulations of the sleeper-asphalt mixture block unit structure, the track stiffness in the DEM model (without lateral constraints) must closely correspond to the FEM-derived results from the previous study (Shi et al., 2024a). Accordingly, the subsequent section will detail the parameter calibration process to achieve alignment between the DEM-predicted track stiffness and the FEM simulation results.

2.2. Model parameter calibration based on track stiffness

Among various contact models in DEM, the parallel contact bonding model stands out as one of the most widely used techniques for simulating asphalt mixtures. In the numerical representation of asphalt mixtures, three primary contact interactions emerge: those occurring between adjacent coarse aggregate particles, the internal cohesive forces within the asphalt mastic itself, and the critical interfacial interactions bridging aggregates and surrounding mastic. The parallel contact bonding model incorporates two distinct sets of mesoscopic parameters: linear contact parameters governing elastic interactions and parallel-bond parameters controlling adhesion failure mechanisms.

The linear contact parameters include Poisson's ratio, effective contact modulus, and stiffness ratio. These parameters are determined based on the physical parameters of constituent materials listed in Table 2, with the resulting values presented in Table 3. Following the calibration of interparticle linear contact parameters in the discrete element framework, the parallel-bond parameters are systematically formulated. These micromechanical descriptors govern the cohesive behaviour of epoxy asphalt mastic matrix and aggregate-mastic interfacial zones, encompassing four critical components: parallel-bond parameters. The parameters mentioned above were determined through indirect tensile strength (ITS) tests in the previous study (Shi et al., 2025). However, laboratory-derived parameters still need to be repetitively calibrated until an acceptable match is reached between the DEM simulations and FEM analysis. It is noteworthy that, in addition to the internal parameters of the asphalt mixture, the mesoscopic parameters at the sleeper-asphalt mixture interface must also be determined. Through investigation of this process, the authors found that when the mortar dosage is 17 kg/m², the shear strength and tensile strength between the epoxy asphalt-cured block and sleeper reach their optimal values of 3.89 and 0.88 MPa, respectively (Wu et al., 2024). Therefore, the strength parameters in the parallel bond model were set according to this bonding strength. Given the comparatively high stiffness of cement concrete, it can be effectively modelled as an aggregate phase. Therefore, the contact parameters between sleeper particles and asphalt-cured block particles can be determined by referring to the meso-scale

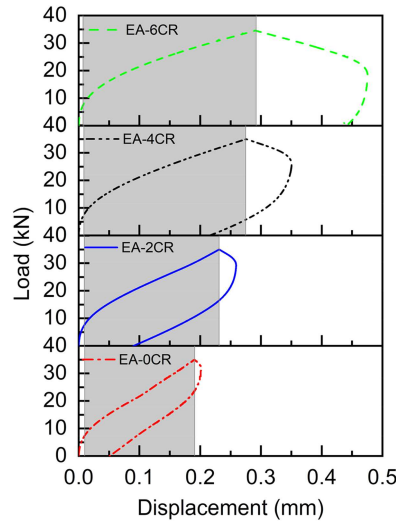


Figure 3. Track stiffness testing of the sleeper-cured block DEM.

interaction parameters established between aggregates and other particles. By comparing the track stiffness obtained from finite element analysis, the parameters are calibrated using inverse analysis methods, so that the deformation characteristics of the discrete element model of the prefabricated sleeper-asphalt mixture block unit structure are similar to those of the finite element structure.

Following calibration of the effective contact modulus, the loading-unloading simulation results for vertical loads on rubberised epoxy asphalt elastic cured trackbed with varying CR contents are presented in [Figure 3](#). The results demonstrate that CR substantially enhance deformation capacity while simultaneously inducing pronounced elastic hysteresis. Based on the displacement-load results of the loading stages according to [Equation 1](#) and [Figure 2](#), the track stiffness of the four types of rubberised epoxy asphalt track bed unit structures can be calculated. The load is applied to the discrete element model of the asphalt ballast unit structure at a rate of 1 kN/s. The loading process continues until reaching 35 kN, followed by unloading. In accordance with the ballast support stiffness calculation method specified in the *Railway Track Design Code* (TB 10082–2017) (China, 2017), the secant stiffness of the load–displacement curve is determined during the loading phase, using the deformations corresponding to 7.5 and 35 kN. The calculation formula is as follows:

$$K = \frac{P_{35} - P_{7.5}}{S_{35} - S_{7.5}}. \quad (1)$$

Where K is the support stiffness, kN/mm; $P_{7.5}$ and P_{35} represent the vertical loads applied to the sleeper at 7.5 and 35 kN, respectively; $S_{7.5}$ and S_{35} denote the corresponding vertical deformations under these load conditions, mm.

The comparison of these values with the stiffness values obtained from finite element numerical simulation is shown in [Table 4](#). The difference between the two is no more than 2.07%, indicating that the discrete element model of the sleeper-solidified block unit structure demonstrates consistent deformation characteristics under zero confining pressure with its deformation response within the track structure. All calibrated contact parameters used for the remainder of this study are listed in [Table 5](#).

2.3. Cyclic loading pattern of train loads

The load of a specific axle weight of the train is shared by five adjacent sleepers. The load acting on the middle sleeper can be characterised by a Gaussian function, and its load-time history curve can be represented by [Equation \(2\)](#) (Xiao et al., 2022):

Table 4. Comparison of track stiffness of prefabricated rubberised epoxy asphalt elastic cured trackbed unit structure under FEM and DEM simulations.

Type	FEM (kN/mm)	DEM (kN/mm)	Difference (%)
EA-0CR	155.6	152.4	2.07
EA-2CR	125.4	123.9	1.23
EA-4CR	101.9	103.0	-1.03
EA-6CR	98.2	96.7	1.53

Table 5. Calibrated model parameters of rubberised epoxy asphalt mixtures with different CR content.

Contact types	Material	Effective modulus (Pa)	Bond effective modulus (Pa)	Bond stiffness ratio	Tensile strength (Pa)	Cohesion strength (Pa)
M-M	EA-0CR	1.87E + 08	3.82E + 06	1.167	1.25E + 06	1.50E + 06
	EA-2CR		3.45E + 06		1.18E + 06	1.41E + 06
	EA-4CR		1.87E + 06		9.50E + 05	1.14E + 06
	EA-6CR		6.93E + 05		3.75E + 05	4.50E + 05
A-A	EA-0CR	5.27E + 10	1.11E + 09	1.125	5.00E + 05	6.00E + 05
	EA-2CR		1.04E + 09		4.70E + 05	5.64E + 05
	EA-4CR		5.31E + 08		3.80E + 05	4.56E + 05
	EA-6CR		2.18E + 08		1.50E + 05	1.80E + 05
A-M	EA-0CR	3.72E + 08	7.82E + 06	1.167	5.00E + 05	6.00E + 05
	EA-2CR		7.69E + 06		4.70E + 05	5.64E + 05
	EA-4CR		3.65E + 06		3.80E + 05	4.56E + 05
	EA-6CR		1.27E + 06		1.50E + 05	1.80E + 05
C-C	EA-2CR	1.66E + 07	3.60E + 05	1.409	3.31E + 05	3.98E + 05
	EA-4CR		1.62E + 05		2.68E + 05	3.21E + 05
	EA-6CR		6.53E + 04		1.06E + 05	1.27E + 05
C-A	EA-2CR	3.31E + 07	7.04E + 05	1.167	3.31E + 05	3.98E + 05
	EA-4CR		3.21E + 05		2.68E + 05	3.21E + 05
	EA-6CR		1.58E + 05		1.06E + 05	1.27E + 05
C-M	EA-2CR	3.04E + 07	6.65E + 05	1.386	3.31E + 05	3.98E + 05
	EA-4CR		3.21E + 05		2.68E + 05	3.21E + 05
	EA-6CR		1.32E + 05		1.06E + 05	1.27E + 05

Note: A, C and M represent the Aggregate, the CR, and the mastic, respectively.

$$P(\nu, t) = P_0 A e^{-\frac{(\nu t)^2}{2w^2}} \quad (2)$$

where P_0 represents the axle load of the train, ν is the speed of the train, t denotes time, and A and w are fitting parameters, both of which are related to the fastener stiffness. Among them, A represents the load-sharing ratio of the middle sleeper. In this paper, referring to the literature (Xiao et al., 2022), the value for ballasted track is taken as 0.36, and the fitted value of w is 0.78. Usually, the distance between two adjacent axles of a bogie is relatively short, so there is an overlapping load area. For the CRH380 high-speed train, the bogie axle spacing is 2.5 m, and the axle load of each axle is 17 t. Therefore, the load generated by a bogie can be expressed as Equation (3):

$$P(\nu, t) = 0.36P_0 \left(e^{-\frac{(\nu t - 1.8)^2}{0.78}} + e^{-\frac{(\nu t - 4.3)^2}{0.78}} \right) \quad (3)$$

The loading frequency is calculated based on the distance between adjacent bogies. For the CRH380 high-speed train, with a bogie axle spacing of 2.5 m and an axle load of 17 t per axle, the loading frequency is determined to be 16.0 Hz. Within one loading cycle, the load acting on the prefabricated sleeper-asphalt mixture block unit structure can be expressed as Equation (4):

$$F(t) = \frac{1}{2}P(\nu, t) + F_{\text{const}} \quad (4)$$

Among them, the speed of 350 km/h is consistent with that used in the finite element analysis. The F_{const} represents the static load of the upper track structure on the asphalt trackbed. Referring to the research in reference (Xiao et al., 2022), a value of 4 kN is adopted. In subsequent studies, the load is applied to the

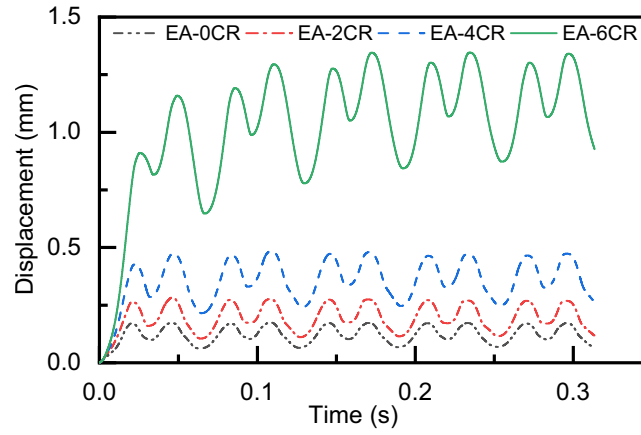


Figure 4. Time-history curve of sleeper under cyclic train loading.

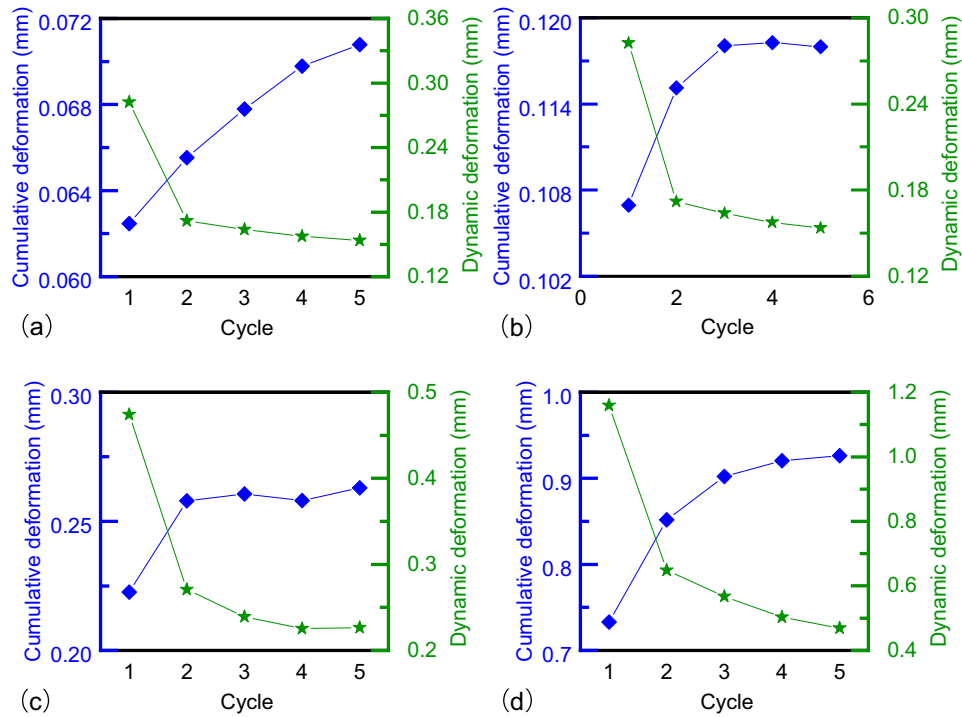


Figure 5. The evolution laws of cumulative deformation and deformation amount with the loading cycles: (a) EA-0CR, (b) EA-2CR, (c) EA-4CR and (d) EA-6CR.

DEM model to simulate repeated train loading, in order to analyse the mechanical response of the new type of prefabricated asphalt trackbed structure under the train loading.

3. Behaviour of cumulative deformation evolution

Under the influence of train loading, the aggregate and CR within the rubberised epoxy asphalt cured block continuously migrate, altering their spatial positions. This migration leads to the formation of a denser mineral system, which in turn reduces the elastic recovery ability of the trackbed and results in cumulative deformation of the trackbed. In this study, after subjecting the unit structure to cyclic loading, the time-course curves of the rail sleeper top under five loading cycles were extracted, as shown in Figure 4.

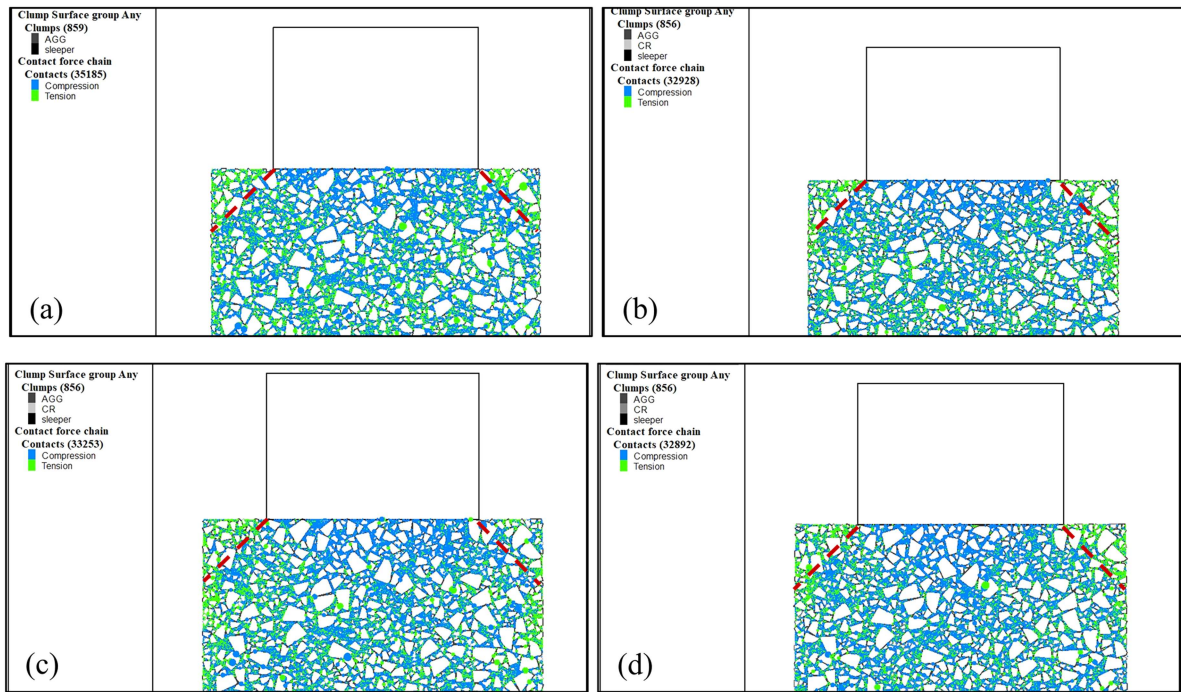


Figure 6. Contact force distribution: (a) EA-0CR, (b) EA-2CR, (c) EA-4CR and (d) EA-6CR.

As depicted in Figure 4, the deformation performance of the rubberised epoxy asphalt trackbed significantly improves with the increased doping of CR. During the first loading cycle, the DEM is in a non-compact state, leading to large deformations in the unit structure. This results in noticeable dynamic and cumulative deformation, with the deformation curve exhibiting two distinct stages: an initial rapid increase followed by stable growth. To quantify the evolution of residual deformation and dynamic deformation with loading cycles, Figure 5 presents the residual deformation at the end of each loading cycle, as well as the deformation difference between the beginning and end of each cycle, i.e. the cumulative and dynamic deformation. As the number of loading cycles increases, the increments in cumulative deformation and dynamic deformation of the asphalt trackbed show a decreasing trend. After entering the third loading cycle, the deformation characteristics of the asphalt trackbed essentially stabilise. At this point, the cumulative deformation of the trackbed is 0.07, 0.12, 0.26, and 0.9 mm, while the dynamic deformation is 0.11, 0.16, 0.24, and 0.57 mm, respectively. When the CR content reaches 6%, the elastic deformation of the asphalt trackbed increases significantly. However, the cumulative deformation is much larger than that of other asphalt trackbeds. This is because the excessive CR particles dominate the deformation characteristics of the skeleton structure, leading to large elastic deformation in the early stages of loading and subsequent particle rearrangement. Once the mineral system forms a new compact state, the CR effectively enhance the elastic dynamic deformation performance of the asphalt trackbed, with dynamic deformation ranging from 0.47 to 0.57 mm. As the mineral particles are bonded by the epoxy asphalt binder to form a cohesive whole, the resistance to cumulative deformation is improved. Meanwhile, the elastic material within the skeleton structure enhances its elastic deformation ability. The initial rapid increase in cumulative deformation experienced during the loading cycle is significantly lower than that of ballasted trackbed (Zhang et al., 2019), although the dynamic deformation amount is similar. This ensures that asphalt trackbed exhibits better elastic deformation without generating substantial cumulative deformation. Polyurethane trackbed structures, which are also a type of cured elastic trackbed, display a similar pattern (Xiao et al., 2022). Research indicates that these structures enter a settlement stabilization stage at the fifth loading cycle, with dynamic deformation in each cycle remaining stable within the range of 0.05–0.1 mm (Xiao et al., 2022). The deformation characteristics of CR-doped epoxy asphalt elastic cured trackbeds demonstrate their ability to provide superior dynamic deformation

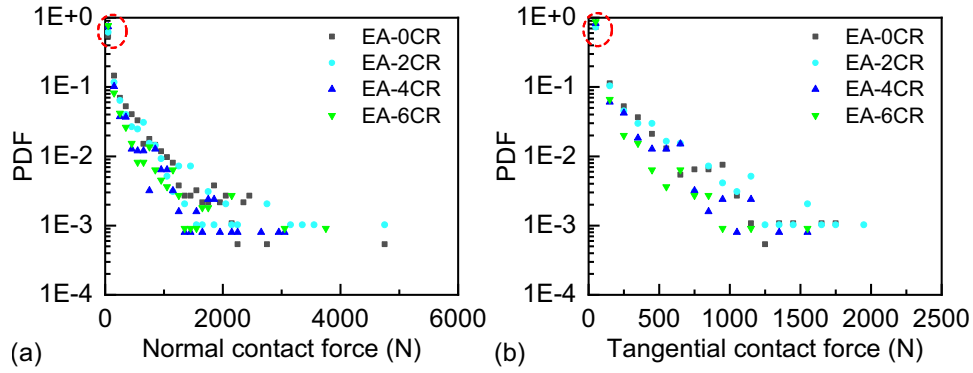


Figure 7. Probability density distribution of coarse aggregate contact forces: (a) normal contact force and (b) tangential contact force.

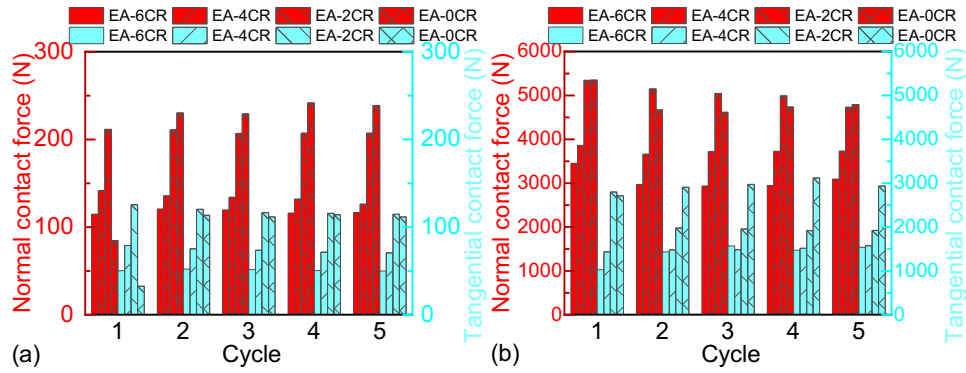


Figure 8. Contact forces between skeleton structure particles: (a) average values and (b) maximum values.

capacity while maintaining minimal cumulative deformation. This characteristic effectively reduces the vibrational impact of track irregularities on the track structure, thereby enhancing travel comfort.

4. Dynamic response characteristics of aggregates/CR

4.1. Contact force analysis

Figure 6 extracts the force chain diagram corresponding to the second load peak moment during the fifth loading cycle, which is used to analyse the spatial distribution of inter-particle contact forces in the block under train loading. In the figures, blue represents compressive forces, while green represents tensile forces. The magnitude of the contact forces is proportional to the size of the circles between particles. Based on the extracted contact force data and the size of the circles, it can be seen that the higher force contacts are mainly located between adjacent coarse aggregates. It can be observed that in the non-contact area of the sleepers at the top of the block (within the range outside the red dashed line), tensile forces are predominant between particles; within a certain depth range directly below the sleepers, compressive forces are mainly dominant, with a small amount of tensile forces in the horizontal direction of particle contact points. The higher contact force chains mainly exhibit a trapezoidal distribution beneath the sleepers.

The distribution law of the contact force magnitude was statistically quantified using the probability density function (PDF). Figure 7 illustrates the probability density of the contact force, with a statistical interval of 100 N. As the centre of the statistical interval increases, the logarithmic form of the contact force probability density exhibits a two-stage pattern: an initial linear decay followed by a gradual approach to a smaller fixed value. The cutoff points for the normal and tangential contact forces in this two-stage pattern are approximately 1250 and 1050 N, respectively.

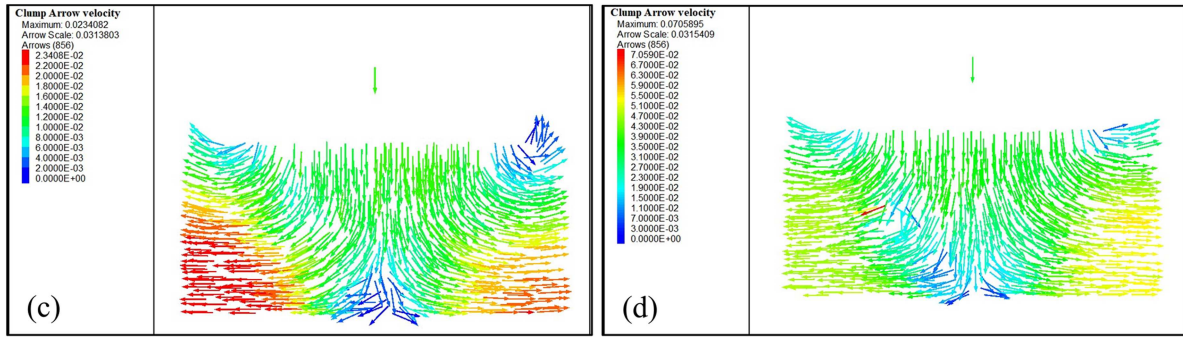


Figure 9. Velocity vector distribution of the coarse aggregate in the framework structure: (a) EA-0CR, (b) EA-2CR, (c) EA-4CR and (d) EA-6CR.

Analysis of the PDF during the linear decay stage reveals that the contact force between coarse aggregate particles primarily falls within the range of 0–100 N. For the four types of asphalt trackbeds, the probability densities of normal and tangential contact forces within this range are 0.55, 0.62, 0.74, 0.77 and 0.73, 0.73, 0.83, 0.87, respectively. These values increase with the addition of more CR. As the probability density rises, the average particle contact force correspondingly decreases. This indicates that large contact forces are relatively rare within the cured block, forming the primary fine-scale load-bearing structure responsible for load transfer in the skeleton. Meanwhile, the majority of contacts function to diffuse aggregate contact forces and stabilise the overall skeleton structure.

As shown in Figure 8, with increasing CR content and loading duration, the average normal and tangential contact forces between particles in the skeleton structure generally exhibit a trend of attenuation. This indicates that CR can effectively mitigate the internal contact forces within the skeleton structure. Overall, the maximum contact forces in both the normal and tangential directions also decrease with increasing CR content. However, during the second to fourth loading cycles, the maximum normal contact force of EA-2CR is slightly higher than that of EA-0CR. This is because, at low CR content levels, the particles can be considered as weak zones within the skeleton structure, resulting in higher contact forces at certain locations. Nevertheless, as the CR content increases to 4%, the degree of rigid-flexible mixing within the mineral system becomes more balanced, leading to a significant reduction in the maximum contact force.

4.2. Spatial distribution of particle velocity and displacement

The spatial distribution of particle motion corresponding to the second load peak moment during the fifth loading cycle within the cured block under train loading is illustrated in Figures 9 and 10, which present the velocity and displacement vector distributions of coarse aggregates or CR, respectively. These figures reveal consistent spatial patterns between velocity and displacement vectors. Particles directly beneath the sleeper, serving as primary load-bearing components, exhibit predominantly vertical downward movement. With decreasing elevation, particle motion gradually transitions into a fan-shaped pattern laterally outward. Near the block's base, particles demonstrate significant horizontal movement, with both velocity and displacement magnitudes increasing toward outside. The middle-lower regions are characterised by tensile force chains, justifying the focus on tensile strain at the block's base in finite element analysis to prevent fatigue cracking (Shi et al., 2024a). This finding supports the need for lateral shoulders in prefabricated rubberised epoxy asphalt trackbed designs to enhance horizontal resistance. Along the vertical centreline, particles maintain downward vertical motion, though with diminishing displacement and velocity due to load attenuation. Notably, tensile-dominated regions near the sleeper's non-contact surface exhibit upward diagonal particle movement, forming semi-vortical vector patterns.

5. Dynamic behaviour of coarse aggregate/CR at different locations

To investigate the vertical movement characteristics of aggregate particles in asphalt-cured blocks under train loading, three monitoring points were established vertically below the sleeper in the DEM (Figure 11). These

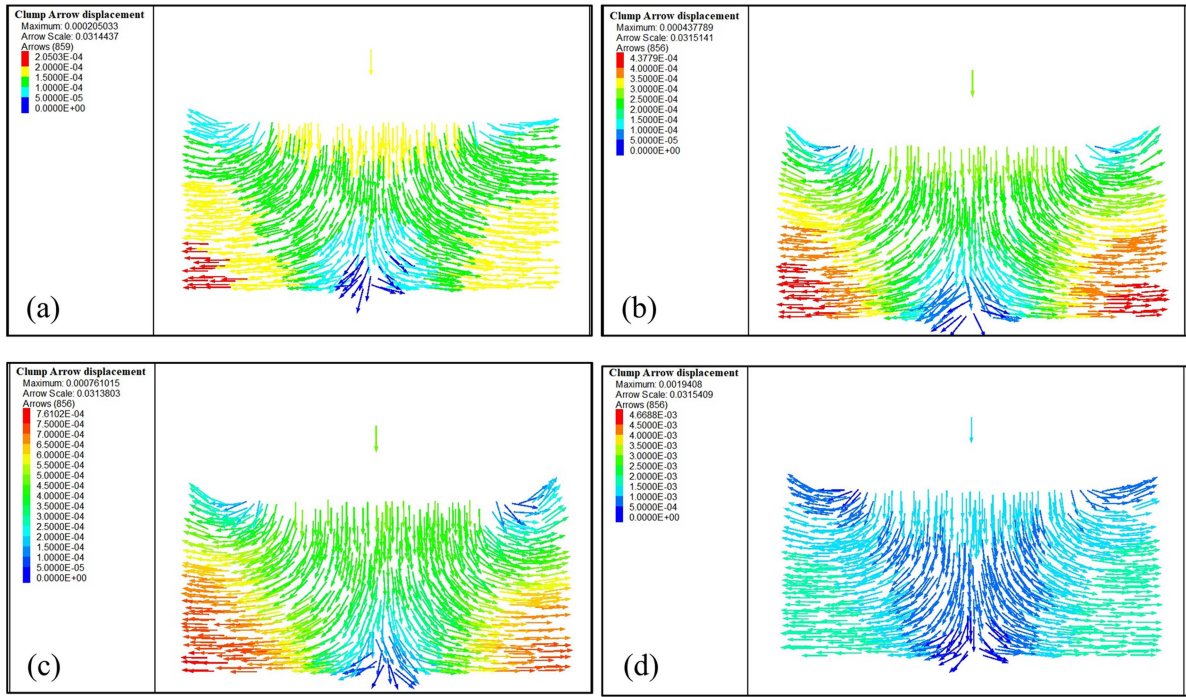


Figure 10. Displacement vector distribution of the coarse aggregate in the framework structure: (a) EA-0CR, (b) EA-2CR, (c) EA-4CR and (d) EA-6CR.

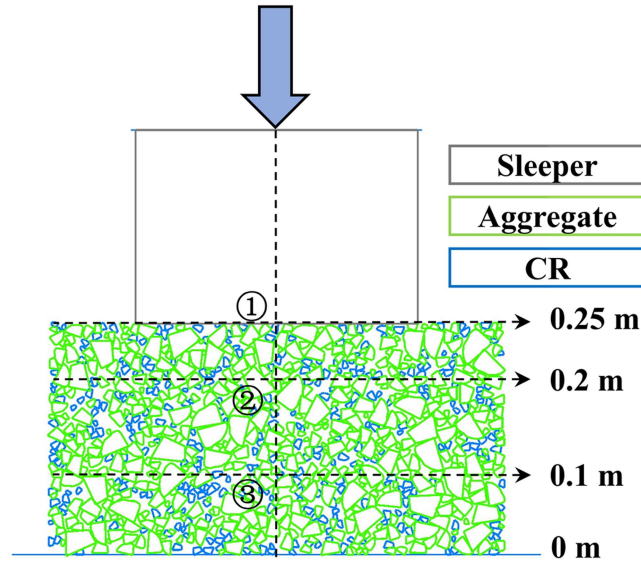


Figure 11. Schematic diagram of particle measurement points at different locations.

points tracked the dynamic response of 4.75–9.5 mm coarse aggregates and CR during loading cycles. The observation points were positioned at: (1) the block surface, (2) 5 cm below the surface, and (3) 10 cm above the block base, creating vertical intervals of 5 cm and 10 cm. For data consistency, particles with comparable volumes were selected for monitoring. When both CR and aggregates were unavailable at an observation point, nearby particles at equivalent height were chosen instead.

5.1. Vertical velocity

Taking the EA-2CR trackbed as an example, Figure 12 illustrates the time curves of vertical velocity for coarse aggregate particles at three observation points within the block. When subjected to train loading,

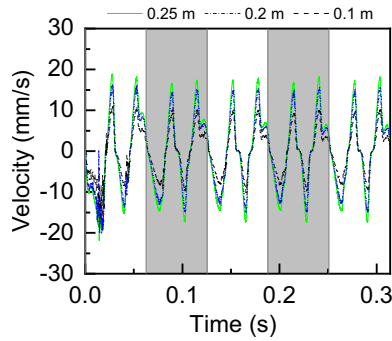


Figure 12. Vertical velocity time-range curves of coarse aggregate particles at different locations in EA-2CR trackbed.

the aggregate particles exhibit a downward movement tendency. During a single loading cycle of the counter frame, the velocity of the aggregate particles follows a pattern of increasing from zero to a maximum value and then gradually returning to zero. Conversely, when the load is removed, the compressive stress within the particles provides an upward movement impetus, resulting in an upward velocity pattern of 'zero-maximum-zero'. Given that each counter frame load cycle includes two peaks, the particles experience three vertical upward and downward movements, which accounts for the four kinetic energy peaks observed in a single loading cycle.

Aggregate particles at other locations beneath the sleeper display a similar velocity pattern, with variations primarily in the magnitude of the velocity amplitude. Particles located at higher heights within the cured block are subjected to greater vibrational loads, leading to correspondingly higher velocity amplitudes. Other trackbed structures exhibit similar patterns in particle velocity parameters, and detailed data will not be reiterated here.

Figure 13 presents a three-dimensional histogram of the maximum downward velocity values of aggregate and CR at each measurement point across loading cycles. The maximum velocity amplitudes for particles moving vertically downward and upward within a single cycle are essentially identical; therefore, this subsection focuses solely on the analysis of downward particle motion. Overall, the maximum velocities decrease with increasing loading cycles and increase with the vertical position of the particles. In the first loading cycle, the discrete element model of the cured block is relatively loose, resulting in somewhat scattered velocity values for the particles. Consequently, this analysis focuses on data from the second to fifth cycles. For the observation point at 0.25 m, the velocity of CR in EA-2CR is higher than that of aggregate particles, with a difference ranging from 2.7 to 4.1 mm/s. In the other two asphalt trackbeds, the velocity of aggregate particles is slightly higher than that of CR, and the velocity difference between the two decreases with increasing rubber particle content. Specifically, the velocity differences for EA-4CR and EA-6CR range from 0.2 to 1.6 mm/s and from 0.1 to 0.3 mm/s, respectively. At the 0.2 m observation point, the velocity differences between aggregate and CR are minimal, with CR exhibiting slightly higher velocities than aggregate particles. At the lowest observation point within the cured block, the velocity difference between the two particle types shows an opposite trend compared to that at 0.25 m, with the largest velocity difference observed in EA-4CR.

To compare the variability of velocities between different particles at the same level, the percentage difference in velocity amplitude between CR and aggregate was calculated, with the results presented in Table 6. Positive values in the table indicate that the velocities of CR exceed those of aggregate particles. As shown in Table 6, in most cases, the velocity variability between aggregate and CR is relatively small. However, a significant difference between the velocities of CR and aggregate particles occurs at the top of the asphalt cured block when the rubber particle content is 2%, with variability ranging from 15.1% to 23.9%. At the 0.2 m level, most CR exhibit higher velocities than aggregate particles. However, the variability in velocity amplitude at the top and bottom of the cured block shows an opposite trend with increasing rubber particle content. This can be attributed to the fact that the modulus of rubber is significantly lower than that of aggregate. When a small amount of CR is introduced into the skeleton structure, it can be considered as a 'weak zone' within the coarse aggregate system. The top of the cured

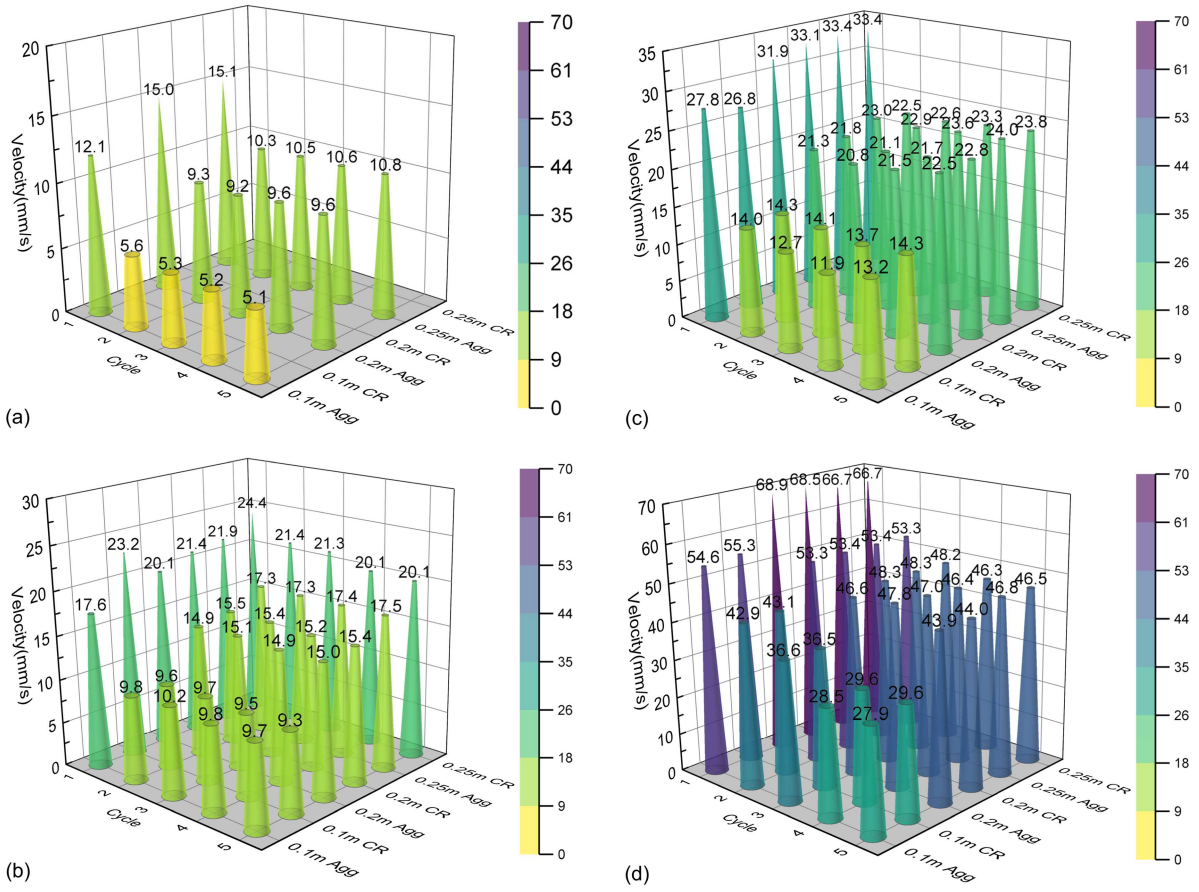


Figure 13. Maximum velocity of downward movement of particles at different positions: (a) EA-0CR, (b) EA-2CR, (c) EA-4CR and (d) EA-6CR (Agg for aggregate).

Table 6. Percentage difference in particle velocity at the same observation point.

Cycle	0.1 m			0.2 m			0.25 m		
	2CR	4CR	6CR	2CR	4CR	6CR	2CR	4CR	6CR
2	-1.5	2.2	0.52	3.6	2.1	0.3	23.9	-2.2	-0.1
3	-5.1	11.2	-0.4	2.1	1.4	3.6	23.1	-1.6	-0.2
4	-4.0	15.2	3.6	2.1	1.0	-1.5	15.9	-1.5	-0.2
5	-4.4	8.4	5.8	2.4	1.3	0.1	15.1	-1.0	-0.6

block is the primary load-bearing layer, and under the impact of the train loading, this weak part of the skeleton structure is compressed, resulting in higher velocities compared to the surrounding aggregate particles. However, as the number of CR increases, the skeletal structure becomes more dominated by CR. When there are more CR with good deformation performance beneath the aggregate particles, the deformation of the CR provides additional space for the aggregate to move downward. Consequently, this results in a larger vertical velocity for the aggregate particles.

5.2. Vertical displacement

Correspondingly, Figure 14 presents the time response curves of vertical displacement for particles at different measurement points. These curves exhibit a temporal variation consistent with the dynamic deformation behaviour of the trackbed. For instance, during the third loading cycle, the maximum displacements of aggregate and CR at the 0.25 and 0.2 m observation points are nearly identical: 0.26, 0.47, and 1.34 mm (0.25 m observation point) versus 0.24, 0.25, and 1.32 mm (0.2 m observation point). At the 0.1 m observation point, the displacement of CR in EA-2CR is slightly larger than that of aggregate

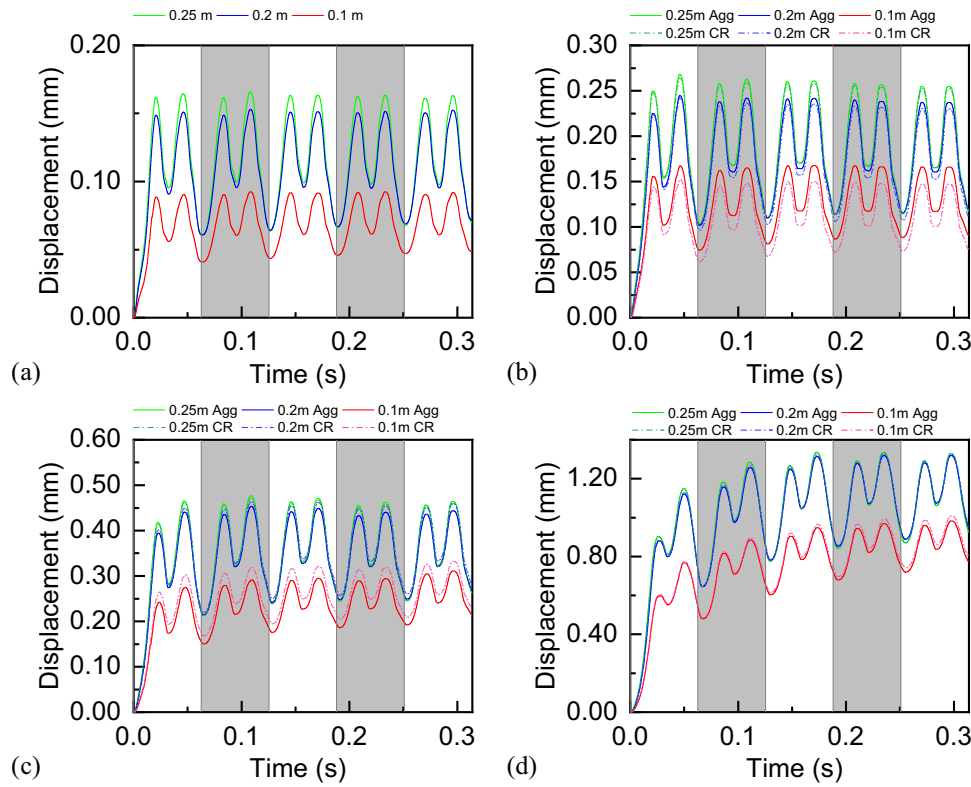


Figure 14. Vertical displacement timescales of particles at different measurement points: (a) EA-0CR, (b) EA-2CR, (c) EA-4CR and (d) EA-6CR.

particles, with a difference of 0.02 mm. However, when the rubber particle content is increased to 4%, the displacement amplitude of aggregate particles becomes larger than that of CR, with a difference of 0.03 mm. In contrast, for EA-6CR, the displacement amplitudes of both aggregate and CR tend to converge at 0.97 mm. At the conclusion of each loading cycle, the unrecovered displacements of particles at the upper two measurement points (0.25 and 0.2 m) are essentially the same and greater than those at the 0.1 m point. This observation indicates that the unrecoverable displacements of particles above the 0.2 m observation point are the primary contributors to the accumulated deformation of the trackbed structure.

To analyse the differential properties of particles moving in the vertical direction, Figures 15 and 16 illustrate the displacement differences among different particles at the same location and among the same type of particles at different locations, respectively. Figure 15 specifically plots the displacement difference between aggregate particles and CR. Since CR is not present in EA-0CR, this section focuses on the motion variability of the other three rubberised epoxy asphalt trackbed. At the 0.25 m observation point, the vertical displacement of aggregate particles is greater than that of CR during the loading stage. However, during unloading, the aggregate displacements in EA-2CR and EA-6CR are smaller than those of CR. This suggests that the recovery of aggregate displacement is better than that of CR, indicating that CR is primarily responsible for the permanent deformation of the upper layer. In contrast, the displacement difference of EA-4CR remains greater than zero throughout the loading process, implying that the aggregate particles exhibit greater vertical movement than CR, which is the main cause of deformation in the top layer of the trackbed.

At the 0.2 and 0.1 m observation points, the vertical displacements of aggregate particles in EA-2CR are larger than those of CR. The displacement difference at 0.1 m is significantly larger than that at 0.2 m and continues to increase with the loading cycle. This indicates that the irrecoverable displacements of aggregate particles at each layer in EA-2CR contribute to the cumulative deformation of the cured block. When the rubber content is increased to 4% and 6%, the displacement difference between aggregate and CR in the cured block becomes more pronounced, with aggregate displacements exceeding those of CR. This is the primary cause of deformation in the top layer of the trackbed, while the cumulative

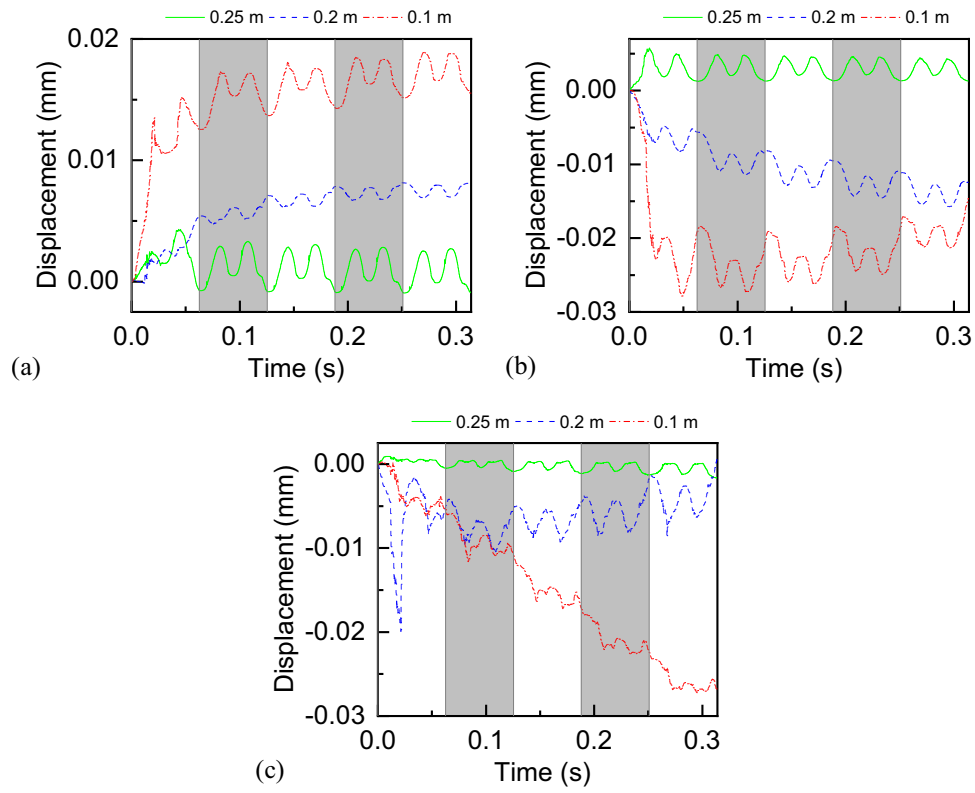


Figure 15. Difference curves of aggregate and rubber particle displacements at the same location: (a) EA-2CR, (b) EA-4CR and (c) EA-6CR.

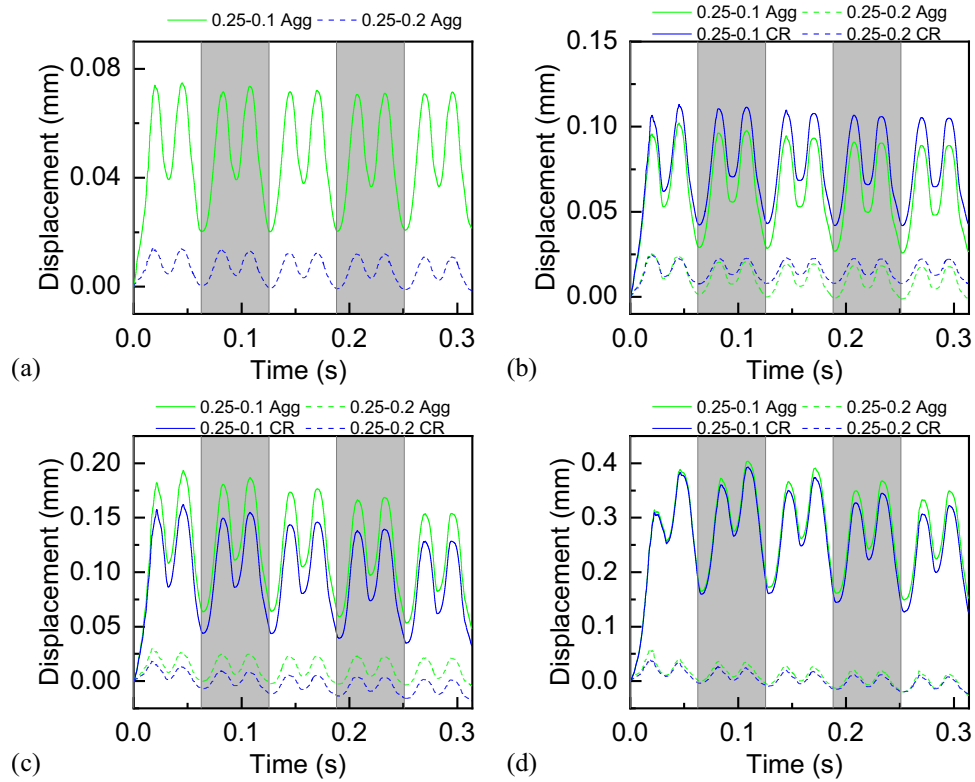


Figure 16. Displacement difference curves of particles at different positions: (a) EA-0CR, (b) EA-2CR, (c) EA-4CR and (d) EA-6CR.

deformation of the lower and middle structures of the cured block is mainly due to the residual displacement of CR. The maximum displacement differences at the 0.2 and 0.1 m observation points are approximately 0.01 and 0.03 mm, respectively.

Figure 16 presents the displacement differences between particles at the 0.25 m observation point and the same type of particles at the other two measurement points, aiming to analyse the motion differences of the same type of particle at varying heights. Given the significant distance between the 0.25 and 0.1 m measurement points, the displacement differences between these points are substantial, with all particles exhibiting displacement differences greater than zero. However, with the exception of the '0.25–0.2 CR' pair in EA-2CR, the displacement differences between particles at the upper two measurement points (0.25 and 0.2 m) showed negative values at low load levels. This indicates that, at these times, the vertical displacement recovery of particles at the 0.25 m point was greater than that of particles at the 0.2 m point. Overall, the displacement differences of CR in EA-2CR are consistently larger than those of aggregate particles. In contrast, EA-4CR and EA-6CR exhibit the opposite pattern. This suggests that the deformation characteristics of the skeleton structure change between EA-2CR and EA-4CR. It can thus be inferred that a rubber particle content of 4% is the critical threshold that alters the phase characteristics of the skeleton structure.

6. Summary and conclusions

This study established a two-dimensional discrete element model for the sleeper-cured asphalt mixture block unit structure. By comparing the results of the sleeper support stiffness in the discrete element and finite element numerical simulations, the contact parameters between particles were adjusted to ensure that the unit structure has relatively consistent deformation characteristics in different numerical simulations. By applying a repeated train load at a speed of 350 km/h to the unit structure, the influence of CR content on the dynamic response of the unit structure's deformation and the contact and motion characteristics of the particles were investigated. The main conclusions are as follows:

1. The stiffness range of the asphalt trackbed DEM is 96.7–152.4 kN/mm. The discrepancy between these results and those obtained from finite element numerical simulations is no more than 2.07%. This close agreement indicates that the deformation response of the railroad tie-cured block unit structure, when unconstrained laterally, is essentially identical in both discrete and finite element models. Consequently, the microscale contact model parameters of the particles in the discrete element model of the unit structure are deemed to be fundamentally reasonable.
2. The dynamic and cumulative deformations of the asphalt trackbed increase significantly with higher CR content. Owing to the adhesive properties of the epoxy asphalt mastic within the skeleton structure, the dynamic deformation stabilises by the third loading cycle. The magnitude of this stabilised dynamic deformation is dependent on the CR content; for instance, the stabilised dynamic deformation of EA-6CR can reach approximately 0.5 mm. Moreover, the combined presence of CR and epoxy asphalt mastic enhances the resistance of the trackbed to cumulative deformation while also enabling it to exhibit substantial dynamic deformation.
3. As the CR content increases, both the average and maximum values of the contact force between particles in the skeleton structure decrease. The contact force is predominantly concentrated within the range of 0–100 N. Moreover, the density of the contact force distribution in this range rises with increasing CR content, indicating that it can effectively mitigate stress within the mineral system. The spatial motion of particles at different locations within the cured block is influenced by the CR content. When the CR content is low, the mechanical properties of the skeleton structure are primarily determined by the aggregate. However, when the content is increased to 4%, the properties are dominated by the elastic material.
4. Based on the variation patterns and differences in velocity and displacement of aggregate and CR at various observation points, it is concluded that a CR content of 4% is the critical threshold for inducing a phase change in the skeleton structure.

Acknowledgements

The authors acknowledge the financial support of the National Natural Science Foundation of China (No.52508484, 52278467, 52078130 and 52378444), Natural Science Foundation of Chongqing (CSTB2025 NSCQ-GPX0872), China Postdoctoral Science Foundation under Grant Number (2025MD774152), the Technology Research and Development Program of China State Railway Group Co., Ltd (P2019G030), Chongqing Talents Program Project (CSTC2024YCJH-BGZX0104), Chongqing Technology Innovation and Application Development Special Key Project (CSTB2022TIAD-KPX0203), Major Projects of the Science and Technology Research Plan of Chongqing Municipal Education Commission (KJZD-M202400704), Chongqing Talent Innovation Demonstration Team (CQYC202203091112), and Joint Training Base Construction Project for Graduate Students in Chongqing (JDLHPYJD2020013, JDLHPYJD2021010).

Author contributions

Chenguang Shi: Conceptualization, Methodology, Formal analysis, Investigation, Writing-original draft, Visualization. You Wu: Methodology, Formal analysis. Guihao Yan: Writing-review & editing. Yang Xu: Writing-review & editing, Formal analysis. Peng Guo: Funding acquisition, Writing-review & editing. Jun Yang: Writing-review & editing, Funding acquisition, Resources, Supervision.

Disclosure statement

No potential conflict of interest was reported by the author(s).

ORCID

You Wu  0000-0001-9807-1832

References

- Alam, M. N., & Hussaini, S. K. K. (2023). Performance of geogrid-reinforced rubber-coated ballast and natural ballast mix under direct shear conditions. *Journal of Materials in Civil Engineering*, 35(9), 1–10.
- Bian, X., Gao, Z., Luo, X., Cai, D., & Chen, Y. (2023). Mesoscale mechanism of asphalt track bed in reducing cyclic settlement of ballast layer under high-speed train traffic loads. *Journal of Transportation Engineering, Part B: Pavements*, 149(1), 1–20.
- Bose, T., Levenberg, E., & Zania, V. (2021). Numerical modeling of a ballastless track mockup based on asphalt. *Construction and Building Materials*, 274, 1–18.
- Bose, T., Zania, V., & Levenberg, E. (2020). Experimental investigation of a ballastless asphalt track mockup under vertical loads. *Construction and Building Materials*, 261, 1–15.
- Charoenwong, C., Connolly, D. P., Costa, P. A., Galvin, P., & Romero, A. (2024). The effect of ballast moisture content and fouling index on railway track settlement. *Transportation Geotechnics*, 45, 1–14.
- China M. R. (2017). *Railway track design code* (Vol. 7). China Railway Publishing House.
- Fang, J., Zhao, C., Cai, C., Chen, C., Shi, C., & Lin, M. (2024). Mechanical behavior and performance evolution of railway ballast track under dynamic stabiliser based on the hybrid mbd-dem simulation. *Transportation Geotechnics*, 46, 1–20.
- Fang, M. J., Hu, T., & Rose, J. G. (2020). Geometric composition, structural behavior and material design for asphalt trackbed: A review. *Construction and Building Materials*, 262, 1–13.
- Fang, M., Hu, T., Fang, K., Hu, Z., Zhang, X., Zhang, J., & Xiao, J. (2022). Mechanical properties of coarse asphalt mixture-paved trackbed under high-speed moving train loads. *Construction and Building Materials*, 357, 1–21.
- Fang, M., Wu, S., Park, D., Chen, H., & Xie, J. (2017). Simple test study on anti-freeze additives selection for railway asphalt mixture (ram) in cold region. *Construction and Building Materials*, 154, 284–293.
- Gruetzmacher, F., Kang, C., & Marx, S. (2025). Historical development of ballastless track systems in Germany. *Construction and Building Materials*, 458, 1–14.
- Gundavaram, D., & Hussaini, S. K. K. (2023a). Application of elastomeric polyurethane in performance improvement of rail ballast subjected to cyclic loading. *Journal of Materials in Civil Engineering*, 35(4), 1–15.
- Gundavaram, D., & Hussaini, S. K. K. (2023b). Elastan-polyurethane treatment for the stability improvement of coal-fouled ballast. *Journal of Materials in Civil Engineering*, 35(8), 1–11.

- Heydari, H., Naseri, R., & Khanie, N. (2024). Investigating the effect of ballast contamination in vertical and shear interlocking stiffness: Experimental and numerical study. *Construction and Building Materials*, 428, 1–13.
- Jin, Z., Zhang, W., Li, Y., & Geng, X. (2025). Numerical studies of ballastless track-embankment vibrations considering track irregularities. *Transportation Geotechnics*, 51, 1–17.
- Jing, G., Qie, L., Markine, V., & Jia, W. (2019). Polyurethane reinforced ballasted track: Review, innovation and challenge. *Construction and Building Materials*, 208, 734–748.
- Khairallah, D., Chupin, O., Blanc, J., Horny, P., & Piau, J.-M. (2022). Simulation of the dynamic response of high-speed line structures composed of granular or bituminous sub-ballast layers and comparison with in situ measurements from embedded instrumentation. *Transportation Geotechnics*, 35, 1–14.
- Lee, S.-H., Choi, C.-Y., Ho Minh Le, T., & Park, D.-W. (2023). Full-scale investigation on inclined ballastless cant track using concrete slab panel at high temperature setting. *Construction and Building Materials*, 366, 1–19.
- Lee, S.-H., Choi, Y.-T., Lee, H.-M., & Park, D.-W. (2016). Performance evaluation of directly fastened asphalt track using a full-scale test. *Construction and Building Materials*, 113, 404–414.
- Lee, S.-H., Eum, K.-Y., Tri Ho Minh, L., & Park, D.-W. (2021). Evaluation on mechanical behavior of asphalt concrete trackbed with slab panel using full-scale static and dynamic load test. *Construction and Building Materials*, 276, 1–20.
- Liu, G., Han, D., Zhao, Y., & Zhang, J. (2022a). Effects of asphalt mixture structure types on force chains characteristics based on computational granular mechanics. *International Journal of Pavement Engineering*, 23(4), 1008–1024.
- Liu, G., Han, D., Zhu, C., Wang, F., & Zhao, Y. (2021). Asphalt-mixture force chains length distribution and skeleton composition investigation based on computational granular mechanics. *Journal of Materials in Civil Engineering*, 33(4), 1–17.
- Liu, G., Huang, T., Lyu, L., Liu, Z., & Ma, C. (2023a). Effective load transfer capacity analysis for asphalt mixture skeleton based on main force chain characteristics and discrete element method. *Journal of Materials in Civil Engineering*, 35(9), 1–17.
- Liu, J., Xiong, Z., Liu, Z., Chen, R., & Wang, P. (2022b). Static and cyclic compressive mechanical characterization of polyurethane-reinforced ballast in a railway. *Soil Dynamics and Earthquake Engineering*, 153, 1–9.
- Liu, Y., Qian, Z., & Zheng, D. (2023b). Influence of coarse aggregate morphology on the mechanical characteristics of skeleton in porous asphalt concrete. *International Journal of Pavement Engineering*, 24(1), 1–10.
- Liu, Y., Qian, Z.-D., Zheng, D., & Huang, Q.-B. (2018). Evaluation of epoxy asphalt-based concrete substructure for high-speed railway ballastless track. *Construction and Building Materials*, 162, 229–238.
- Luan, Y., Chen, T., Ma, T., Ma, Y., & Wang, N. (2021). Fracture performance analysis of cold-recycled mixture based on dem precise modeling. *China Journal of Highway and Transport*, 34(10), 125–134. <https://zgglxb.chd.edu.cn/CN/10.19721/j.cnki.1001-7372.2021.10.010>
- Malisetty, R. S., & Indraratna, B. (2024). Critical speed of ballasted railway tracks: Influence of ballast and subgrade degradation. *Transportation Geotechnics*, 46, 1–13.
- Paz, C., Suarez, E., Vence, J., Paradela-Rodriguez, J., Montero-Cubillo, N., & Estaire, J. (2024). Advanced approach for assessing the degradation of railway ballast particles through detailed 3d scanning. *Construction and Building Materials*, 436, 1–12.
- Ramirez Cardona, D., Di Benedetto, H., Sauzeat, C., Calon, N., & Rose, J. G. (2020). Designs, application and performances of asphalt/bituminous trackbeds in European, Asian, and African countries. *Transportation Research Record*, 2674(11), 245–262.
- Shi, C., Guo, P., Zhu, H., Gao, J., & Yang, J. (2025). Mesoscopic mechanical analysis of the effect of crumb rubber content on rubberized epoxy asphalt mixture under indirect tensile discrete element method simulation. *International Journal of Pavement Engineering*, 5, 1–18.
- Shi, C., Sun, X., Wang, T., Wu, Y., Liu, S., Wang, H., Yang, J., Xu, Y., & Qie, L. (2022). Numerical analysis of dynamic behavior of bi-block precast asphalt trackbed for high-speed railway. *Construction and Building Materials*, 342, 1–12.
- Shi, C., Wu, Y., Fuentes, R., Fan, Y., Zhou, Y., Fu, C., & Yang, J. (2024a). Volumetric mix-design modification and vibration attenuation analysis of rubberised epoxy asphalt track for railway. *Road Materials and Pavement Design*, 26(8), 1890–1913.
- Shi, C., Wu, Y., Wang, H., Liu, S., Liu, P., Yang, J., & Huang, W. (2024b). Analysis of crumb rubber content influence on damage evolution and pattern recognition of rubberised epoxy asphalt mixture using acoustic emission techniques. *International Journal of Pavement Engineering*, 25(1), 1–15.
- Shi, C., Zhang, H., Wang, T., Zhou, Y., Liu, S., Wang, H., Yang, J., Xu, Y., & Qie, L. (2021). Design and performance evaluation of bi-block precast rubberized epoxy asphalt trackbed for railway. *Construction and Building Materials*, 313, 1–11.
- Wang, N., Li, Q., Zhang, L., & Wang, J. (2025). Anti-aging and durability performance of pavement markings under multifactor coupling effects. *Construction and Building Materials*, 484, 1–11. <https://www.sciencedirect.com/science/article/pii/S0950061825019919>
- Wang, N., Zhang, C., Ma, T., Nadimi, S., Chen, F., & Ding, X. (2023). Mechanical insights into the behavior of cement stabilized aggregates during compaction and failure using smart aggregate: Experiments and dem simulations. *Construction and Building Materials*, 399, 1–14.

- Wang, T., Shi, C., Yu, Y., Xu, G., Liu, S., Wang, H., Yang, J., Gong, M., Xu, Y., & Qie, L. (2022). Mechanical properties evaluation of crumb rubber asphalt mixture for elastic trackbed. *Construction and Building Materials*, 331, 127048. <https://www.sciencedirect.com/science/article/pii/S0950061822007310>
- Wu, Y., Shi, C., Yu, Y., Chen, H., Fan, Y., Wang, H., Yang, J., & Huang, W. (2023). Dynamic behavior of precast epoxy asphalt track bed for transition zone in high-speed railway: A numerical approach. *Transportation Geotechnics*, 40, 1–14.
- Wu, Y., Zhou, Y., Shi, C., Yu, Y., Fan, Y., Cai, X., Zhou, Y., Wang, H., Gong, M., Hong, J., Yang, J., & Huang, W. (2024). Interlayer bonding quality evaluation of sleeper-asphalt block composite structure applied to asphalt elastic cured track bed. *Construction and Building Materials*, 415, 1–18.
- Xiao, H., Ling, X., Wang, M., Fang, S.-W., & Wang, H.-Y. (2022). Mechanical behaviour and energy evolution of polyurethane-mixed ballast under revised bonding constitutive model. *Construction and Building Materials*, 320, 1–23.
- Xiao, J.-L., Jing, P., Yu, S.-X., & Wang, P. (2020). Analysis on the track quality evolution law of polyurethane-reinforced ballasted track in high-speed railway. *Proceedings of the Institution of Mechanical Engineers Part F-Journal of Rail and Rapid Transit*, 235(8), 993–1005.
- Xiao, X., Cai, D., Lou, L., Shi, Y., & Xiao, F. (2021). Application of asphalt based materials in railway systems: A review. *Construction and Building Materials*, 304, 1–22.
- Xiong, Z., Liu, J., Wang, P., Liu, G., Xiao, J., & Yu, S. (2021). Field dynamic performance testing and analysis of polyurethane track and ballasted track in a high-speed railway. *Journal of Civil Structural Health Monitoring*, 11, 867–877.
- Xu, Y., Yu, W., Qie, L., Sheng, Z., & Li, Y. (2024). Grading analysis of resilient polyurethane solidified ballasted bed using the discrete element method. *Construction and Building Materials*, 457, 1–12.
- Zhang, X., Xie, J., Jing, G., & Xu, C. (2023). A novel laboratory investigation to characterize the mechanical behaviors of polyurethane-ballast bonds under complex stress states. *Transportation Geotechnics*, 40, 1–12.
- Zhang, X., Zhao, C., & Zhai, W. (2019). Importance of load frequency in applying cyclic loads to investigate ballast deformation under high-speed train loads. *Soil Dynamics and Earthquake Engineering*, 120, 28–38.
- Zhang, Y., Chen, W., Luo, S., Wang, W., Yuan, Q., & Sheng, X. (2024). Experimental investigation and soft bond modelling analysis on mechanical behaviours of foamed polyurethane solidified ballast. *Construction and Building Materials*, 440, 1–16.
- Zhao, L., Jiang, D., Zhao, G., Sun, J., & Yang, G. (2024). Experimental study on the dynamic characteristics of bi-block ballastless track under the combined action of vehicle load and temperature gradient. *Construction and Building Materials*, 438, 1–14.